lubricants

MDPI

Article

On the Film Stiffness Characteristics of Water-Lubricated Rubber Bearings in Deep-Sea Environments

Liwu Wang [2], Qilong Zhao [3], Wei Feng [1,*] and Guo Xiang [1,4,*]

[1] College of Mechanical and Intelligent Manufacturing, Chongqing University of Science and Technology, Chongqing 401331, China
[2] School of Marine Technology and Equipment, Hainan University, Haikou 570228, China; 997205@hainanu.edu.cn
[3] State Key Laboratory of Mechanical Transmission for Advanced Equipment, Chongqing University, Chongqing 400044, China; 202307021092t@stu.cqu.edu.cn
[4] School of Mechanical Engineering, Southwest Jiaotong University, Chengdu 610031, China
* Correspondence: weifeng@cqust.edu.cn (W.F.); guoxiang@swjtu.edu.cn (G.X.)

Abstract

Rubber bearings play a critical role as core components within the transmission systems of marine equipment. Investigating the evolution of their water-film stiffness coefficient under deep-sea conditions can provide deeper insights into the dynamic characteristics of water-lubricated transmission systems. Employing a viscoelastic mixed-lubrication framework designed for water lubricated rubber bearings, this paper examines the necessity of accounting for rubber hyperelasticity and extreme subsea conditions (high pressure and low temperature) when analyzing the water-film stiffness coefficient of such bearings (at a depth of 1000 m, the relative error in the k_{xz} component between the linear viscoelastic model and the visco-hyperelastic model reaches as high as 18.41%.). On this basis, the influence of subsea environments together with rotational velocity on the water-film stiffness coefficient is further investigated, and the dependence of the dimensionless critical mass on the eccentricity ratio for water-lubricated rubber bearings operating under deep-ocean conditions is explored. The results provide a theoretical analysis tool for evaluating the water-film stiffness coefficient of subsea rubber bearings, and offer guidance for the forward design of water-lubricated rubber bearings applied in deep-sea service.

Keywords: water-lubricated rubber bearings; visco-hyperelastic mixed lubrication; dynamic coefficient; deep-sea environment

check for updates

Received: 20 September 2025
Revised: 13 October 2025
Accepted: 15 October 2025
Published: 17 October 2025

Citation: Wang, L.; Zhao, Q.; Feng, W.; Xiang, G. On the Film Stiffness Characteristics of Water-Lubricated Rubber Bearings in Deep-Sea Environments. *Lubricants* **2025**, *13*, 451. https://doi.org/10.3390/lubricants13100451

Copyright: © 2025 by the authors. Licensee MDPI, Basel, Switzerland. This article is an open access article distributed under the terms and conditions of the Creative Commons Attribution (CC BY) license (https://creativecommons.org/licenses/by/4.0/).

1. Introduction

The oceans span roughly 70.8% of Earth's surface and are abundant in natural resources [1]. Progress in marine technologies and equipment is fundamental to resource development [2]. As the development of marine resources expands into deeper and more remote areas, there is an increasing demand for exploration and extraction technologies. As critical components in the propulsion systems of ships, submarines, naval vessels, and underwater robots, water-lubricated rubber bearings are crucial for ensuring the stability, safety, and efficiency of these systems. Thus, improving the operational efficiency of water-lubricated rubber bearings under deep-sea conditions is a key scientific issue that should be addressed to support technological advancements and equipment development for marine exploration and utilization.

Water-lubricated rubber bearings offer outstanding environmental friendliness, simple structure, ease of maintenance, corrosion resistance, impact resistance, low noise, long service life, and good maintainability. However, owing to the low viscosity of water, the tribo-pair in water-lubricated rubber bearings often operates in mixed lubrication or even dry friction under extreme service conditions. Experimental evidence consistently demonstrates notable differences in hydrodynamic pressure distribution between water-lubricated rubber bearings and conventional rigid or low-deformation bearing systems. Owing to the generally low hydrodynamic pressures that develop, such bearings are more susceptible to operating in the mixed lubrication regime. This condition can lead to increased friction, accelerated wear, as well as elevated vibration and noise levels [3,4]. Furthermore, the operational behavior of these bearings is strongly influenced by a range of factors, including operational parameters (e.g., speed and load) [5], structural design features—such as material properties, radial clearance, and groove geometry—along with surface characteristics [6,7].

Numerical simulation is extensively utilized as a powerful tool to analyze the mixed-lubrication behavior in water-lubricated rubber bearings. Gong et al. [8] proposed an elastic deformation evaluation-coefficient method and developed an elastohydrodynamic lubrication (EHL) model for micro-groove water-lubricated bearings. Sander et al. [9] investigated bearing friction behavior during the transition from hydrodynamic to mixed lubrication, providing a solid basis for validating isothermal EHL simulation methods. Based on preceding research, Deng et al. [10–12] developed a comprehensive statistical-based mixed lubrication approach specifically designed for journal bearings, enabling a detailed analysis of the frictional and dynamic characteristics associated with water-lubricated bearings.

For large bearings, the maximum film thickness greatly exceeds the minimum nominal film thickness, so local turbulence may arise. Using the Ng–Pan turbulence model, Lv et al. [13,14] and Ouyang et al. [15,16] proposed an unsteady mixed-lubrication simulation approach that accounts for local turbulence. Their analysis showed that, under mixed lubrication, local turbulence increases the minimum film thickness, reduces the friction coefficient, and lowers the rotor speed at which the system transitions to hydrodynamic lubrication. Furthermore, Xie et al. [17,18], Han et al. [19] and Song et al. [20] investigated the behavior and critical features of water-lubricated bearings under extreme operating environments. Their work introduced an innovative multi-physics coupled lubrication model that incorporates rotor dynamic effects along with surface micro-topography, elucidating the mechanism by which surface morphology and operating conditions influence transitions between lubrication regimes. In parallel, Zhao et al. [21] used the finite difference method to simulate, systematically, multiple characteristics of water-lubricated bearings. Wu et al. [22] employed fractal theory to describe the surface topographies of the bearing and journal, and by combining a fractal contact model with the average Reynolds equation, established a mixed-lubrication friction model based on fractal theory. Following earlier developments, a data-driven approach was proposed by Ouyang et al. [23] to simulate the lubrication distribution in water-lubricated bearings, thereby offering an innovative framework for the design and optimization of these systems. Through a systematic evaluation of mesh density effects, Shen et al. [24] improved both the accuracy and computational efficiency of fluid–structure interaction (FSI) simulations. Leveraging this improved approach, they further analyzed the effects of operational conditions and structural parameters on the lubrication behavior of rubber–plastic bearings. Kuang et al. [25] employed a speed-dependent Stribeck friction model to characterize the dynamic friction between a rubber bearing and a rudder stock, and investigated the stability of the nonlinear system via the Lyapunov indirect method. Chen et al. [26] and Shi et al. [27] established a transient

thermo-elastohydrodynamic lubrication (TEHL) model that accounts for the influence of eccentricity ratio, enabling a detailed investigation into the spatial and temporal evolution of the bearing's tribological characteristics.

In the foregoing studies on water-lubricated bearings, deformations induced by hydrodynamic and contact pressures were generally assumed to be purely elastic or elasto-plastic [28,29]. It is noteworthy, however, that the contact, deformation, and friction mechanisms of rubber exhibit typical visco-hyperelastic characteristics, which differ significantly from classical solid contact mechanics and friction laws [30,31]. As a result, the complex modulus of rubber shows pronounced nonlinearity as well as temperature and frequency dependence under complex stress states, giving rise to intricate mixed-lubrication behavior in water-lubricated rubber bearings. In deep-sea environments in particular, limited material strength can lead to large deformations under pressure, increasing the bearing clearance and substantially changing the mixed-lubrication behavior of the bearing system and the characteristics of the water-film stiffness coefficient. In earlier studies, a mixed-lubrication model specifically designed for water-lubricated rubber bearings was established by our research group, incorporating the visco-hyperelastic properties of the material [32]. Subsequently, by incorporating deep-sea environmental factors, the model was extended to analyze mixed-lubrication performance under such conditions [33].

Scholars have significantly advanced the numerical investigation of mixed lubrication in water-lubricated bearings, but most studies are limited to elastic or elasto-plastic contact models, making it difficult to capture the water-film stiffness characteristics of rubber-based water-lubricated bearings under extreme underwater conditions. Therefore, building upon the previously proposed visco-hyperelastic lubrication framework, this paper aims to explore in detail the evolutionary behavior of the water-film stiffness characteristics of rubber bearings operating in deep-sea environments.

2. Mathematical Model

Figure 1 schematically illustrates the viscoelastic mixed lubrication behaviors for rubber bearings lubricated by water in subsea environments. Figure 1a illustrates the physical configuration of the water-lubricated rubber bearing (BTG water-lubricated rubber bearing), which consists of a rubber liner bonded to a naval brass sleeve. Figure 1b depicts the coordinate system established for the bearing. During operation, the water-lubricated bearing system typically operates under eccentric conditions due to external load excitation. Owing to the low viscosity of water, a relatively thin fluid film is required to generate sufficient hydrodynamic pressure. When the hydrodynamic pressure within the water film is insufficient to support the applied load, asperity contact occurs between the bearing and journal surfaces (defined by a ratio of water-film thickness to root mean square surface roughness less than 4), as shown in Figure 1c. Furthermore, the deep-sea environment imposes extreme conditions such as high hydrostatic pressure and low temperature, which may induce structural deformation and alterations in material properties of the bearing, as demonstrated in Figure 1d,e.

2.1. Visco-Hyperelastic Contact Model

2.1.1. Fractional-Order Derivative Visco-Hyperelastic Model

In this study, the hyperelastic behavior of rubber is characterized using the two-parameter Mooney–Rivlin strain energy density model, which can be written as:

$$W_h = k_1(I_1 - 3) + k_2(I_2 - 3) \tag{1}$$

where W_h is the strain energy density, and k_1 and k_2 represent parameters obtained from single-axis experimental evaluations; under single-axis loading conditions, the invariants

can be expressed as: $I_1 = \varepsilon + 2\varepsilon^{-1}$, $I_2 = \varepsilon^{-2} + 2\varepsilon$, in which ε denotes the principal stretch ratio, defined as $\varepsilon = h_a/h_b$, with h_a and h_b indicating the initial and deformed dimensions.

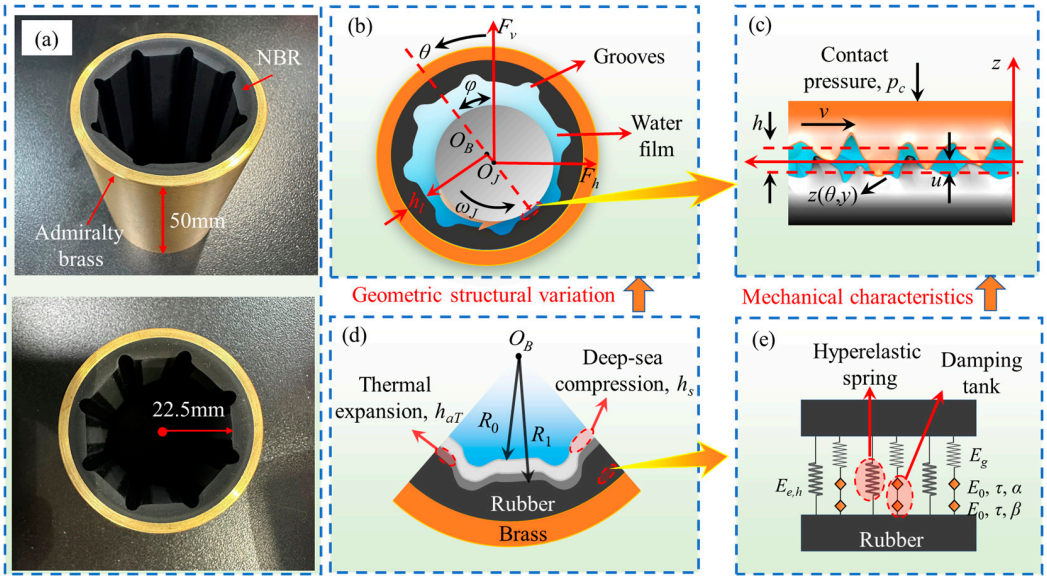


Figure 1. Schematic representation of viscoelastic mixed lubrication for water-lubricated rubber bearings in subsea environments. (**a**) BTG water-lubricated rubber bearing; (**b**) Coordinate system for WLRBs; (**c**) Diagram of rubber in contact with a rigid rough surface; (**d**) Compression and thermal expansion under deep-sea conditions; (**e**) Fractional visco-hyperelastic model.

The static elastic modulus is formulated as:

$$E_{e,h} = \frac{d}{d\varepsilon}\left(2\left(\frac{\partial W_h}{\partial I_1}\left(\varepsilon - \frac{1}{\varepsilon^2}\right) + \frac{\partial W_h}{\partial I_2}\left(1 - \frac{1}{\varepsilon^3}\right)\right)\right) \tag{2}$$

when the strain ε approaches 1, $E_{e,h}$ represents the equilibrium elastic modulus as t tends to infinity, where t represents time.

The viscoelastic behavior of rubber is modeled using an enhanced fractional Zener constitutive formulation, as introduced by Luo et al. [34].

Within the frequency spectrum, the complex modulus $E^*(\omega)$ can be formulated as follows:

$$E^*(\omega) = E'(\omega) + \mathrm{i}E''(\omega) \tag{3}$$

where ω corresponds to angular frequency, $E'(\omega)$ and $E''(\omega)$ represent the storage and loss modulus. These components are determined as follows:

$$E'(\omega) = \frac{E_{e,h}E_g^2\lambda_1 + (E_{e,h} + E_g)E_0^2(\omega\tau)^{2(\alpha+\beta)} + (2E_{e,h} + E_g)E_gE_0(\omega\tau)^{\alpha+\beta}\lambda_2}{E_0^2(\omega\tau)^{2(\alpha+\beta)} + E_g^2\lambda_1 + 2E_gE_0(\omega\tau)^{\alpha+\beta}\lambda_2} \tag{4}$$

$$E''(\omega) = \frac{E_g^2E_0(\omega\tau)^{\alpha+\beta}\lambda_3}{E_0^2(\omega\tau)^{2(\alpha+\beta)} + E_g^2\lambda_1 + 2E_gE_0(\omega\tau)^{\alpha+\beta}\lambda_2} \tag{5}$$

where

$$\begin{cases} \lambda_1 = (\omega\tau)^{2\alpha} + (\omega\tau)^{2\beta} + 2(\omega\tau)^{\alpha+\beta}\cos((\alpha-\beta)\pi/2) \\ \lambda_2 = (\omega\tau)^{\beta}\cos(\alpha\pi/2) + (\omega\tau)^{\alpha}\cos(\beta\pi/2) \\ \lambda_3 = (\omega\tau)^{\beta}\sin(\alpha\pi/2) + (\omega\tau)^{\alpha}\sin(\beta\pi/2) \end{cases} \tag{6}$$

E_g corresponds to the glass modulus in the instantaneous response limit (as $t \to 0$); the parameters E_0 and τ denote the stiffness and mean relaxation period of the spring-pot

element. The fractional orders α and β, both lying in the range (0,1), characterize the spring-pot behavior.

The temperature-dependent variation in the composite modulus of rubber materials can be approximated using the Williams-Landel-Ferry [33] equation:

$$E^*(\varepsilon, \omega, T) = E^*(\varepsilon, \omega a_T / a_{T0}, T_0) \tag{7}$$

where

$$\log(a_T) \approx -8.86 \frac{T - T_g - 50}{51.5 + T - T_g} \tag{8}$$

where T_g denotes the glass transition temperature and is defined as the maximum temperature of $\tan\delta_0(T)$ measured at a frequency of ω = 0.01 Hz. The value of T_g adopted in this paper is −63.8 °C [33].

2.1.2. Visco-Hyperelastic Contact Pressure

In the present work, the mechanical contact model proposed by Persson [35,36] is employed to describe the sliding interaction involving a rubber medium and a hard, rough surface. In the modeling of WLRBs, the sliding velocity v is assumed to remain constant and is restricted exclusively to the circumferential direction (θ-direction).

Within Fourier space, the relation linking normal stress $p(m,n,\omega)$ with surface deformation $u(m,n,\omega)$ for a viscoelastic material is formulated as [37–39]:

$$p(m, n, \omega) = M^{-1}(m, n, \omega) u(m, n, \omega) \tag{9}$$

The viscoelastic solid response function, denoted as $M(m,n,\omega)$, is determined through the following expression:

$$M(\mathbf{q}, \omega) = -2 \frac{1 - v_p^2}{E^*(\omega)} \frac{S(2qh_l)}{|\mathbf{q}|} \tag{10}$$

and

$$u(m, n, \omega) = \frac{1}{(2\pi)^3} \int\int\int u(\theta, y, t) R_1 e^{-i(mR_1\theta + ny - \omega t)} \mathrm{d}\theta \mathrm{d}y \mathrm{d}t \tag{11}$$

The surface displacement in the time domain is denoted by $u(\theta,y,t)$, where θ and y represent circumferential and axial directions, respectively. v_p represents Poisson's ratio. The wave vector is defined as $\mathbf{q}$ = (m,n), with angular frequency $\omega = qv$. Here, $S(qh_l)$ serves as a correction factor, with h_l representing the rubber layer thickness. Under the condition $qh_l \longrightarrow \infty$, the value of $S(qh_l)$ approaches unity.

The mean surface displacement, denoted as u_m, resulting from viscoelastic contact is expressed as follows:

$$u_m(\theta, y) = \int_h^\infty z\phi(z)dz \Big/ \int_h^\infty \phi(z)dz - h \tag{12}$$

where h corresponds to the water-film thickness, z represents the direction along the film thickness, and $\phi(z)$ denotes the probability distribution of surface height.

2.1.3. Visco-Hyperelastic Contact Load

The interface pressure $p_c(\theta,y)$ acting on an individual asperity is obtained through the inverse Fourier transformation in the following form:

$$p_c(\theta, y) = \int\int p_c(m, n) e^{i(mR_1\theta + ny)} \mathrm{d}m \mathrm{d}n \tag{13}$$

The total contact load, denoted as F_c, is expressed through the following relation:

$$F_c = S_i \int \int_{\Omega_0} R_1 p_c(\theta, y) \mathrm{d}\theta \mathrm{d}y \tag{14}$$

The domain Ω_0 corresponds to the contact region of an individual asperity, defined by the condition: $0 \leq ((R_1\theta)^2 + y^2)^{1/2} \leq l/2$, in which R_1 is the inner radius of the rubber bearing. Meanwhile, S_i represents the overall asperity count engaged within the contact interface between the rubber bearing and the journal.

2.2. Lubrication Model

Under mixed lubrication regimes, the average Reynolds equation can be employed to calculate the hydrodynamic pressure at the interface, which is expressed as follows [40]:

$$\frac{\partial}{R_1^2 \partial\theta}\left(\phi_\theta \frac{\rho h^3}{12\eta_0}\frac{\partial p_h}{\partial\theta}\right) + \frac{\partial}{\partial y}\left(\phi_y \frac{\rho h^3}{12\eta_0}\frac{\partial p_h}{\partial y}\right) = \frac{\omega_J}{2}\left(\phi_c \frac{\partial h}{\partial\theta} + \sigma\frac{\partial \phi_s}{\partial y}\right) \tag{15}$$

The journal bearing's inner radius is denoted as R_1, and η_0 represents the water density. The journal's rotational velocity is indicated by ω_J. In the circumferential (θ) and axial (y) directions, the pressure flow factors are described by ϕ_θ and ϕ_y, respectively. Additionally, ϕ_c [41] and ϕ_s [40] correspond to the contact flow factor and shear flow factor, respectively. p_h is the hydrodynamic pressure of water film.

Within the depth interval from 0 to 2000 m, the viscosity of seawater is predominantly influenced by temperature. Beyond 2000 m, however, pressure emerges as the principal factor governing viscosity [42]. The dynamic viscosity of seawater across different depths is determined through the empirical relation given below [42]:

$$\eta = \begin{cases} \eta_0 \exp(-0.03579T + 0.617), & h_w < 2000\,\mathrm{m} \\ \eta_0 \exp(0.00273 p_s + 0.919), & h_w \geq 2000\,\mathrm{m} \end{cases} \tag{16}$$

where h_w denotes the seawater depth, η_0 is the seawater viscosity at ambient temperature, p_s is the static pressure of the seawater, and T is the temperature of the seawater.

In this study, Equation (15) is solved under the Reynolds cavitation boundary condition, formulated as follows:

$$\begin{cases} p_h(\theta, 0) = 0 \\ p_h(\theta_0, y) = 0, \partial p_h(\theta_0, y)/\partial\theta = 0 \end{cases} \tag{17}$$

The angular position at which the water film ruptures along the circumferential direction is denoted by θ_0.

2.3. Film Thickness Equation

The deformation of rubber is strongly nonlinear, which makes the variation in the water-film clearance in WLRBs complex and calls for careful treatment. Under deep-sea conditions, the water-film clearance with elastic deformation taken into account can be written as:

$$h(\theta, y) = h_g(\theta, y) + h_d(\theta, y) + h_{gro}(\theta, y) + h_T(\theta, y) \tag{18}$$

where $h_d(\theta,y)$ is the elastic deformation; $h_{gro}(\theta,y)$ is the groove depth, $h_T(\theta,y)$ is the thermal expansion of the rubber bush. and $h_g(\theta,y)$ refers to the geometric clearance, given by:

$$h_g(\theta, y) = (C_0 + h_{aT} + h_s)[1 + \kappa_e \cos(\theta - \varphi)] \tag{19}$$

The initial clearance in the radial direction between the bearing and the journal is represented by C_0. The eccentricity ratio and attitude angle are denoted as κ_e and φ, respectively. Additionally, h_{aT} accounts for the thermal distortion of the WLRB resulting from variations in the surrounding temperature.

The thermal deformation $h_T(\theta,y)$ is evaluated based on the methodology introduced by Kuznetsov et al. [43].

$$h_{aT} = \alpha_r(T - T_0)h_l \tag{20}$$

where α_r denotes the thermal expansion coefficient of the rubber; T_0 represents the temperature of the sea surface.

During steady-state operation of a WLRB, the load-supporting region exhibits minimal variation, resulting in a state of quasi-persistent contact. Under this condition, as $t\to\infty$ and $\omega\to0$, the viscoelastic modulus simplifies to $E^*(\varepsilon, \omega, T_0) = E_{e,h}(\varepsilon)$. The elastic deformation h_d, generated through both hydrodynamic and contact pressures, is formulated using the relation below [44,45]:

$$h_d = \frac{h_l(p_c + p_h)}{2\zeta(\varepsilon_0) + \lambda_0(\varepsilon_0)} \tag{21}$$

where the Lamé parameters ζ and λ_0 are derived as follows:

$$\zeta(\varepsilon_0) = \frac{E_{e,h}(\varepsilon_0)}{2(1+\upsilon_p)} \tag{22}$$

$$\lambda_0(\varepsilon_0) = \frac{\upsilon_p E_{e,h}(\varepsilon_0)}{(1+\upsilon_p)(1-2\upsilon_p)} \tag{23}$$

Similarly, the radial deformation h_s of the WLRB induced by seawater pressure can be written as:

$$h_s = \frac{h_l p_s}{2\zeta(\varepsilon_0) + \lambda_0(\varepsilon_0)} \tag{24}$$

where ε_0 denotes the compressive strain of the rubber in the deep-sea environment, $\varepsilon_0 = (h_l - h_s - h_{aT})/h_l$; h_{aT} is the deformation induced by changes in the ambient temperature.

2.4. Solution of Stiffness and Damping Coefficients of Water Film

Through classical perturbation theory, a first-order Taylor series expansion around the journal's steady-state position (x_0, z_0) in the lubrication film enables derivation of the subsequent perturbed average Reynolds equation:

$$\left[\frac{\partial}{R_1^2\partial\theta}\left(\phi_\theta\frac{h_0^3}{12\eta}\frac{\partial}{\partial\theta}\right) + \frac{\partial}{\partial y}h_0^3\left(\phi_y\frac{1}{12\eta}\frac{\partial}{\partial y}\right)\right]p_\vartheta = B_\vartheta(hx, hz, hx', hz') \tag{25}$$

where h_0 denotes the water-film thickness at the equilibrium position. $p_\vartheta(\vartheta = hx, hz, hx'$ and $hz')$ represents the perturbed hydrodynamic pressure, where $\vartheta = hx, hz$ corresponds to the displacement-induced perturbed hydrodynamic pressure, and $\vartheta = hx', hz'$ represents the velocity-induced perturbed hydrodynamic pressure. The right-hand term of Equation (25), namely $B_\vartheta(\vartheta = hx, hz, hx'$and $hz')$, can be calculated as:

$$\begin{cases} B_{hx} = \frac{\omega_J}{2}\left(\cos\theta - \frac{3\phi_\theta\sin\theta}{h_0}\frac{\partial h_0}{\partial\theta} - \frac{\phi_\theta h_0^3}{4\eta R_1^2}\frac{\partial p_{h0}}{\partial\theta}\frac{\partial}{\partial\theta}\left[\frac{\sin\theta}{h_0}\right]\right) \\ B_{hz} = -\frac{\omega_J}{2}\left(\sin\theta + \frac{3\phi_\theta\cos\theta}{h_0}\frac{\partial h_0}{\partial\theta} - \frac{\phi_\theta h_0^3}{4\eta R_1^2}\frac{\partial p_{h0}}{\partial\theta}\frac{\partial}{\partial\theta}\left[\frac{\cos\theta}{h_0}\right]\right) \\ B_{hx'} = \sin\theta \\ B_{hz'} = \cos\theta \end{cases} \tag{26}$$

The perturbed hydrodynamic pressure is obtainable through numerical computation of Equation (26). It should be noted that this study involves the analysis of critical mass, thus requiring the calculation of both water-film stiffness coefficients and damping coefficients. Therefore, although this paper emphasizes the comparative analysis of water-film stiffness characteristics, it is also necessary to present the calculation process for water-film damping coefficients. Subsequently, the water film's stiffness and damping parameters can be evaluated by Equations (27) and (28), respectively, which are expressed as follows:

$$\begin{bmatrix} k_{xx} & k_{xz} \\ k_{zx} & k_{zz} \end{bmatrix} = \begin{bmatrix} \int_0^L \int_0^{2\pi} p_{hx} \cos(\theta) R_1 \mathrm{d}z\mathrm{d}\theta & \int_0^L \int_0^{2\pi} p_{hz} \cos(\theta) R_1 \mathrm{d}z\mathrm{d}\theta \\ \int_0^L \int_0^{2\pi} p_{hx} \sin(\theta) R_1 \mathrm{d}z\mathrm{d}\theta & \int_0^L \int_0^{2\pi} p_{hz} \sin(\theta) R_1 \mathrm{d}z\mathrm{d}\theta \end{bmatrix} \tag{27}$$

$$\begin{bmatrix} c_{xx} & c_{xz} \\ c_{zx} & c_{zz} \end{bmatrix} = \begin{bmatrix} \int_0^L \int_0^{2\pi} p_{hx'} \cos(\theta) R_1 \mathrm{d}z\mathrm{d}\theta & \int_0^L \int_0^{2\pi} p_{hz'} \cos(\theta) R_1 \mathrm{d}z\mathrm{d}\theta \\ \int_0^L \int_0^{2\pi} p_{hx'} \sin(\theta) R_1 \mathrm{d}z\mathrm{d}\theta & \int_0^L \int_0^{2\pi} p_{hz'} \sin(\theta) R_1 \mathrm{d}z\mathrm{d}\theta \end{bmatrix} \tag{28}$$

The stiffness and damping coefficients in this paper are dimensionless according to the following formulas:

$$\begin{bmatrix} K_{xx} & K_{xz} \\ K_{zx} & K_{zz} \end{bmatrix} = \left(\frac{c}{R_1}\right)^3 \frac{30}{\pi \omega_J \eta L} \begin{bmatrix} k_{xx} & k_{xz} \\ k_{zx} & k_{zz} \end{bmatrix} \tag{29}$$

$$\begin{bmatrix} C_{xx} & C_{xz} \\ C_{zx} & C_{zz} \end{bmatrix} = \left(\frac{c}{R_1}\right)^3 \frac{1}{\eta L} \begin{bmatrix} c_{xx} & c_{xz} \\ c_{zx} & c_{zz} \end{bmatrix} \tag{30}$$

where L denotes the bearing length. The dimensionless load can be formulated as:

$$W_h = \left(\frac{c}{R_1}\right)^2 \frac{30 F_f}{\pi \omega_J \eta R_1 L} \tag{31}$$

where F_f denotes the hydrodynamic load. The critical mass coefficient of the bearing can be calculated as:

$$M_L = \frac{(M_a)_{cr}}{\varsigma_v W_h} \tag{32}$$

where

$$(M_a)_{cr} = \frac{C_{zz}K_{xx} + C_{xx}K_{zz} - C_{xz}K_{zx} - C_{zx}K_{xz}}{C_{zz} + C_{xx}} \tag{33}$$

and

$$\varsigma_v = \frac{(K_{xx} - (M_a)_{cr}) * (K_{zz} - (M_a)_{cr}) - K_{xz}K_{zx}}{C_{xx}C_{zz} - C_{xz}C_{zx}} \tag{34}$$

2.5. Numerical Algorithm

This study employs numerical simulations conducted using Microsoft Visual Studio as the development environment, with programs implemented in the Fortran programming language. Figure 2 shows the calculation procedure for analyzing the visco-hyperelastic hydrodynamic lubrication and dynamic characteristics of the water film. On this basis, the rubber deformation, the initial elastic modulus of the rubber, and the seawater viscosity are evaluated, thereby determining the clearance in the WLRB. Next, the transient averaged Reynolds equation (Equation (15)) is solved through a finite-difference numerical scheme to calculate the hydrodynamic pressure field, whereas the contact pressure field is obtained through Persson's multiscale contact model (Equation (13)). Based on the obtained pressure

distributions, the resulting deformation field of the bearing is computed through the governing equations, and this feedback further modifies the complex viscoelastic properties of the rubber material (Equations (2) and (21)–(23)).

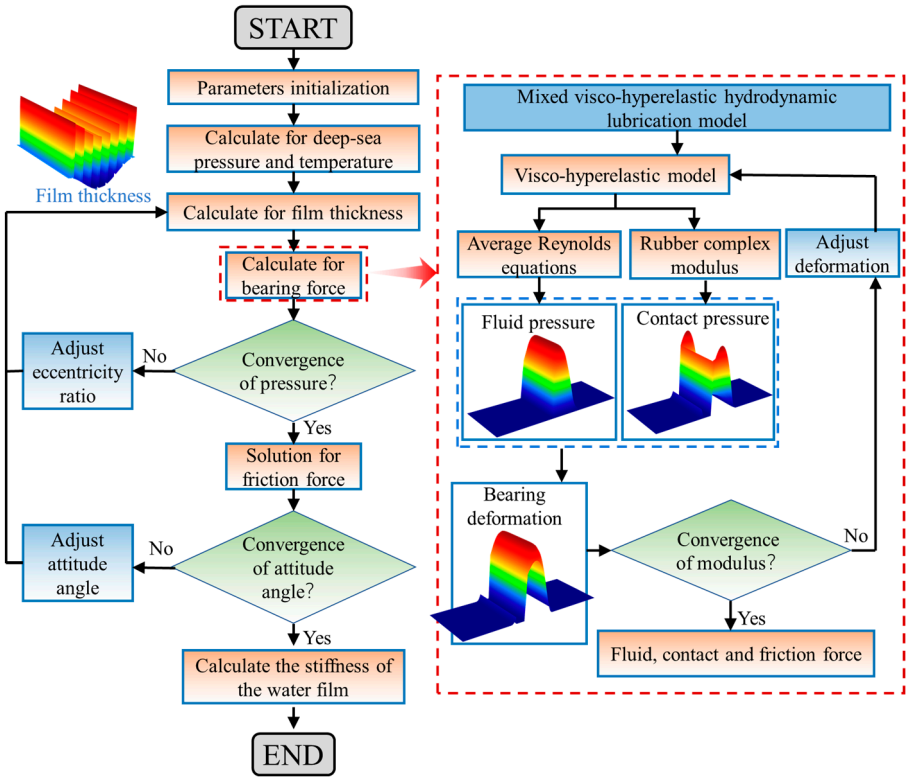


Figure 2. Calculation procedure for analyzing the visco-hyperelastic hydrodynamic lubrication and dynamic characteristics of the water film.

Once the rubber's complex elastic modulus together with the hydrodynamic pressure satisfy the bearing's load capacity requirement, the load-carrying capability is calculated through integration of both hydrodynamic and contact pressures (Equation (14)); otherwise, the eccentricity ratio is adjusted until both values converge. If the convergence tolerance (10^{-4}) is fulfilled for the fluid load, contact load, and external load, the water-film stiffness coefficient is then obtained (Equations (25)–(29)). If not, the eccentricity ratio should be further tuned until the load balance satisfies the convergence condition. In the same way, once the angular position reaches the specified convergence tolerance, the computation ends; if not, the angular position is updated iteratively until the required convergence criterion is reached.

In the numerical implementation of the model, the repetitive procedure for solving the averaged Reynolds equation employs a convergence tolerance of 1×10^{-5}. The corresponding fluid pressure convergence criterion is formulated as follows:

$$\frac{\sum_{j=1}^{n}\sum_{k=1}^{m}\left|p_{h(j,k)}^{(new)} - p_{h(j,k)}^{(old)}\right|}{\sum_{j=1}^{n}\sum_{k=1}^{m}\left|p_{h(j,k)}^{(old)}\right|} \leq 1.0 \times 10^{-5} \tag{35}$$

The iterative modification of the angular orientation in both horizontal and vertical directions is carried out under the joint effect of hydrodynamic and contact forces. Its value is determined through the following expression:

$$\varphi^{(new)} = \varphi^{(old)} - \text{arctg}\left(\frac{F_h}{F_v}\right) \tag{36}$$

The convergence criterion for the attitude angle is defined as follows:

$$\varphi_{error} = \left|\varphi^{(new)} - \varphi^{(old)}\right| / \varphi^{(new)} \leq 1.0 \times 10^{-3} \tag{37}$$

The convergence criterion applied to the complex viscoelastic modulus of the rubber is specified as below:

$$E^*(\varepsilon, \omega, T)_{error} = \frac{\left|E^*(\varepsilon, \omega, T)^{(new)} - E^*(\varepsilon, \omega, T)^{(old)}\right|}{E^*(\varepsilon, \omega, T)^{(new)}} \leq 1.0 \times 10^{-6} \tag{38}$$

Table 1 presents the simulation parameters utilized in this study.

Table 1. Simulation settings for this study.

Parameters	Value	Parameters	Value
Bearing inner radius, R_1	22.5 mm	Relaxation time, τ	5×10^{-8} s
Rubber thickness, h_l	2.5 mm	Bearing Poisson ratio, υ_p	0.47
Bearing length, L	50 mm	Fractional order, α	0.17
Radial clearance, C_0	0.1 mm	Fractional order, β	0.77
Specific pressure	0.1 MPa	Seawater depth, h_w	0–1000 m
Shaft rotational speed, ω_J	300~900 rpm	Ambient temperature, T_a	5–28 °C
Equilibrium modulus, $E_{e,h}$	30 MPa	Instantaneous modulus, E_g	2.3 GPa
Modulus of spring pot, E_0	3.0 GPa	Number of grooves	8
Groove depth, h_{gro}	1.0 mm	Groove width	3.53 mm
Hyperelastic parameters, k_1	1.47 MPa	Seawater density, ρ	1050 kg/m^3
Hyperelastic parameters, k_2	4.02 MPa	Reference temperature, T_0	20 °C
Characteristic scale coefficient	3.0×10^{-8} m	Fractal dimension, H	1.5
Constant, γ	1.5		

3. Results and Discussion

3.1. Model Verification

3.1.1. Grid Independence Verification

This section verifies the independence of the average Reynolds equation and water-film stiffness with respect to grid size. When the axial grid number exceeds 31 and the circumferential grid number exceeds 320, key parameters such as maximum fluid pressure, contact load ratio, and water-film stiffness coefficient for the WLRB converge to stable values. Specifically, when the number of axial grid points was increased from 31 to 41, concurrently with an increase in circumferential grid points from 320 to 400, the maximum relative error for the maximum fluid pressure was 0.34%; for the contact load, it was 0.91%; and for the friction coefficient, it was 0.79%. Thus, a grid density with more than 320 circumferential divisions and more than 31 axial divisions ensures sufficient accuracy in simulating the mixed lubrication performance and water-film stiffness of the bearing. Furthermore, grid resolution significantly influences computational efficiency in numerical simulations. Considering both accuracy and efficiency, this study adopts a grid configuration of 320 × 31 (circumferential × axial) for the WLRB.

3.1.2. Verification of Water-Film Stiffness Coefficient

Previous studies have experimentally verified the validity of the isothermal visco-hyperelastic mixed-lubrication model [32]. In this work, the accuracy of the water-film

stiffness coefficient predicted by the present model is assessed through comparison with published literature. Since both theoretical and experimental results for the dynamic coefficients of water-lubricated rubber bearings that incorporate visco-hyperelasticity are still unavailable, the current validation disregards the influence of bearing shell deformation to focus on the evaluation of the water-film dynamic coefficient. As illustrated in Figure 3, the dimensionless stiffness coefficient of the water film calculated from this model is compared against Hamrock's numerical outcomes [46] across various eccentricity ratios. The investigated bearing is a journal type with two axial grooves positioned 180° apart, each spanning 20° circumferentially and exhibiting a length-to-diameter ratio of 2.0. Results indicate that the predicted dimensionless stiffness coefficients show strong agreement with Hamrock's findings [46], with only minor deviations that remain within acceptable margins. Hence, the comparison with Hamrock's numerical results [46] provides sufficient evidence to confirm the reliability of the water-film stiffness coefficient obtained from the present model.

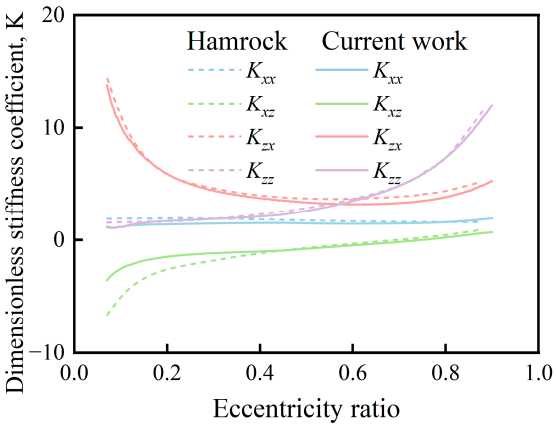


Figure 3. Comparison of dimensionless stiffness coefficients at different eccentricities.

3.2. Comparative Analysis of Linear Viscoelastic and Visco-Hyperelastic Constitutive Models

According to Equation (2), because of the hyperelasticity of rubber, its static modulus increases with increasing compressive strain, which significantly affects the contact and deformation behaviour of WLRBs. As a consequence, the water-film distribution changes, thereby influencing lubrication performance such as the fluid-pressure and heat-flux distributions, and hence the water-film stiffness coefficient.

Deep-sea environments are generally marked by extreme hydrostatic pressures and consistently low temperatures. Within a certain range, seawater temperature decreases with increasing depth [47], as shown in Figure 4a, while seawater pressure increases with depth.

The seawater temperature utilized in the model calculations was derived from polynomial fitting of Hartoko's data, as shown in Figure 4a. The resulting polynomial function is as follows:

$$T = \begin{cases} 28, & h_w \le 30\,\mathrm{m} \\ \left(\begin{array}{l} 31.57 - 0.15h_w + 3.69 \times 10^{-4}h_w^2 - 4.49 \times 10^{-7}h_w^3 \\ +2.56 \times 10^{-10}h_w^4 - 5.48 \times 10^{-14}h_w^5 \end{array}\right), & 30\,\mathrm{m} < h_w < 1600\,\mathrm{m} \\ 3.3, & h_w \ge 1600\,\mathrm{m} \end{cases} \quad (39)$$

Under these extreme conditions, significant structural compression occurs in WLRBs, resulting in measurable changes to their geometric configuration and viscoelastic properties, as illustrated in Figure 4b–d. Moreover, when rubber's hyperelasticity is disregarded, the static modulus of WLRBs remains unaffected by the deep-sea environment.

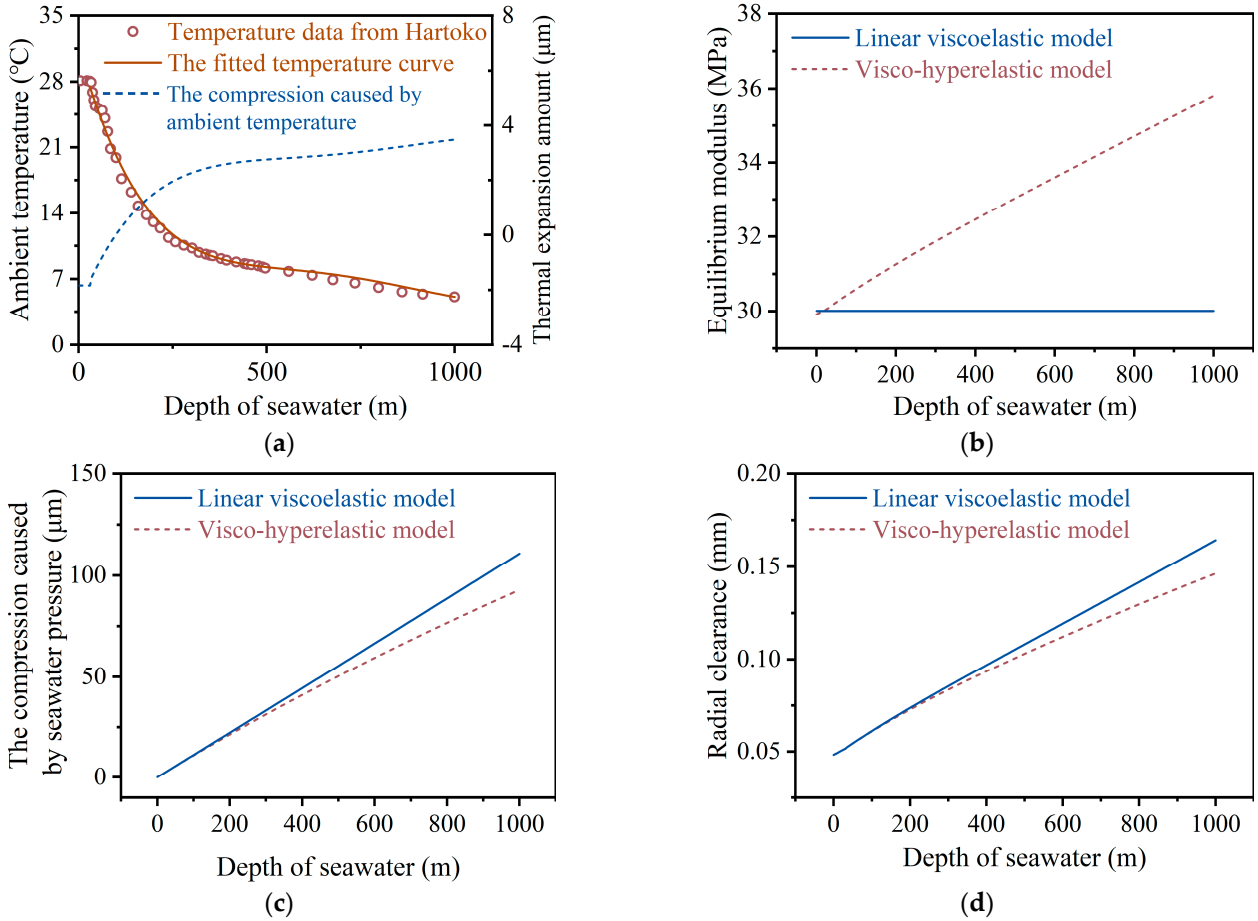


Figure 4. Effects of Seawater Depth on Ambient Temperature and Structural/Physical Properties of Water-Lubricated Rubber Bearings: (**a**) Seawater temperature and thermal expansion; (**b**) Equilibrium modulus; (**c**) Compressive deformation under seawater pressure; (**d**) Radial clearance.

At the sea surface, where the ambient temperature is higher and the seawater pressure is lower, thermal expansion causes the static modulus in the visco-hyperelastic model to be smaller than that in the viscoelastic model. At greater depths, the combined effect of higher seawater pressure and lower temperature results in greater compressive deformation of rubber bearings lubricated with water; meanwhile, the static elastic modulus within the visco-hyperelastic model gradually increases progressively, thereby mitigating the amount of compression induced by seawater pressure, as shown in Figure 4c. Consequently, at larger depths, the visco-hyperelastic model yields a larger static modulus and a smaller radial clearance. Moreover, with increasing depth, the differences between the visco-hyperelastic and viscoelastic models in terms of static modulus and radial clearance grow progressively, as illustrated in Figure 4b,d.

According to Equation (2), owing to the hyperelasticity of rubber, its static modulus increases with increasing compressive strain, which in turn markedly affects the contact and deformation behaviour of water-lubricated rubber bearings. As a result, the water-film distribution changes, thereby influencing lubrication performance such as the hydrodynamic pressure, and hence the water-film stiffness coefficient. Therefore, to gain deeper insight into the mechanism by which hyperelasticity affects mixed lubrication and the lubricant film stiffness coefficient for rubber bearings lubricated with water, this section compares mixed lubrication performance and the water-film stiffness coefficient predicted by linear viscoelastic as well as visco-hyperelastic constitutive models at varying seawater depths.

Figure 5 shows a comparison of the hydrodynamic pressure distributions given by the linear viscoelastic formulation and the visco-hyperelastic formulation at various sea-water depths. It can be observed that, as sea-water depth increases, the radial clearance in the water-lubricated rubber bearing increases progressively, leading to a decrease in the load-bearing area of the bearing and thus requiring a larger pressure distribution to sustain operation. Meanwhile, the viscosity of seawater increases with depth, enhancing the hydrodynamic effect for water-lubricated rubber bearings. Consequently, as depth increases, the maximum fluid stress increases gradually, whereas the area over which the pressure is distributed narrows, as shown in Figure 5.

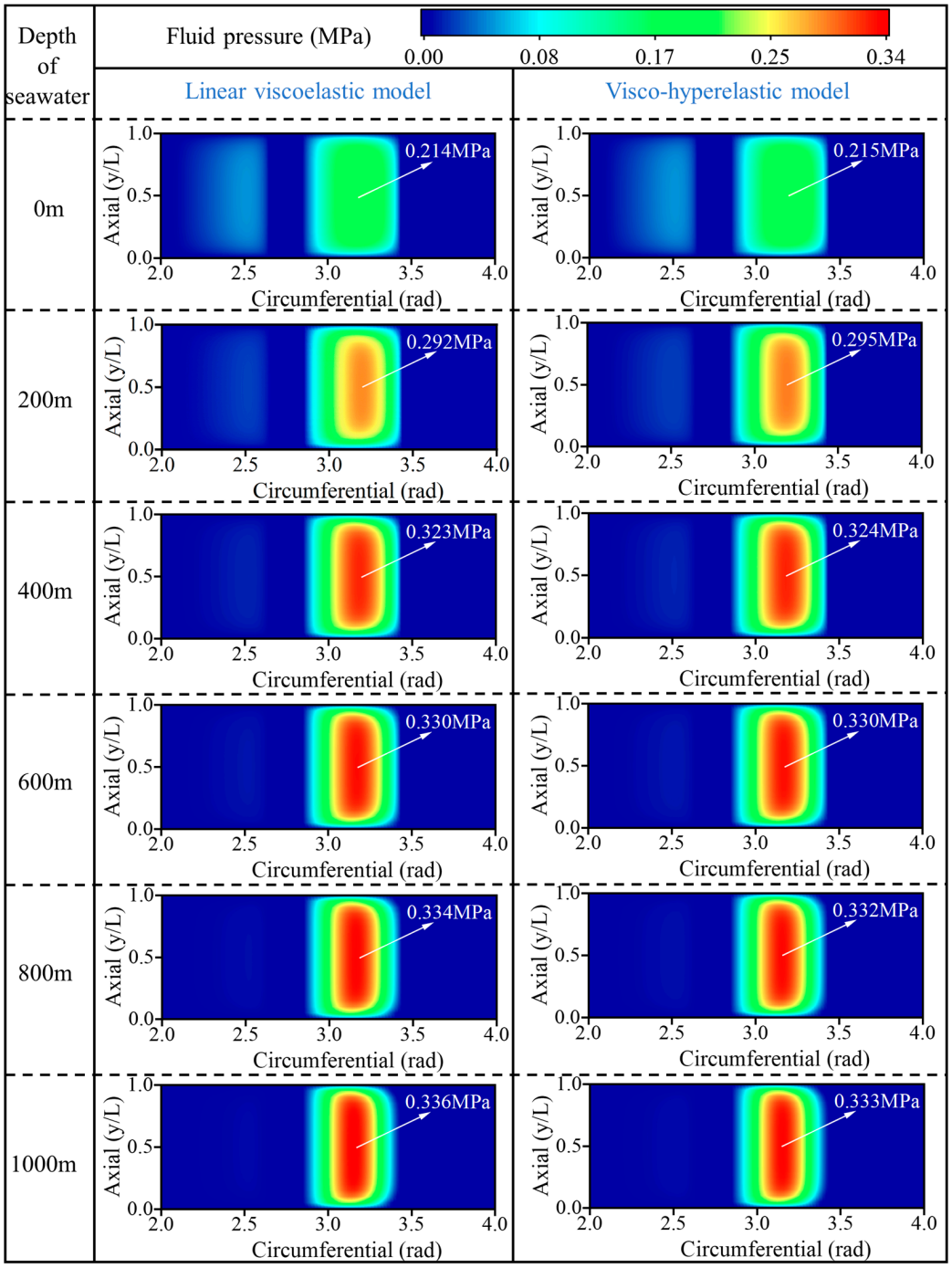


Figure 5. Comparative analysis of water-film pressure distributions derived from the viscoelastic and visco-hyperelastic model approaches across varying seawater depths.

In addition, at shallow seawater depths, the peak fluid dynamic pressure estimated through the linear viscoelastic formulation is lower than that obtained with the visco-hyperelastic model; at greater depths, the trend reverses, and the discrepancy between the two models becomes more pronounced with increasing depth.

Figure 6 presents a comparative analysis of the contact load proportion and maximum elastic deformation calculated by the linear viscoelastic framework and the visco-hyperelastic formulation under varying seawater depths. As seawater depth increases, the contact load proportion derived from both models initially decreases and subsequently rises. Furthermore, the linear viscoelastic model yields a higher contact load proportion at shallower seawater depths, which becomes comparatively lower at larger seawater depths, as illustrated in Figure 6a.

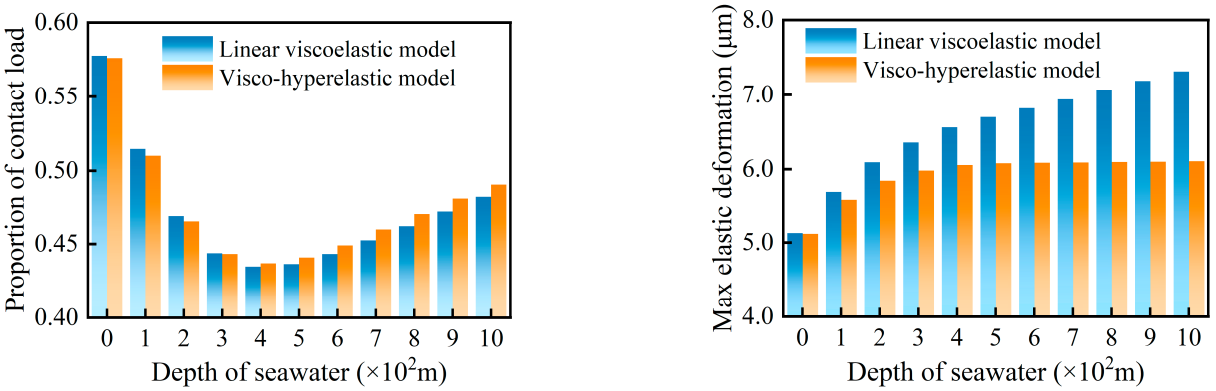


Figure 6. Comparative analysis of the contact load proportion and maximum elastic deformation calculated by viscoelastic and visco-hyperelastic model approaches under varying seawater depths: (**a**) proportion of contact load; (**b**) maximum elastic deformation.

In the visco-hyperelastic model, the rubber static modulus increases with increasing seawater depth, which, to some extent, weakens the elastic deformation jointly induced by hydrodynamic and asperity-related pressures. Therefore, in the visco-hyperelastic constitutive framework, while the peak hydrodynamic pressure demonstrates a monotonic increase with depth, the corresponding maximum elastic deformation undergoes an initial rapid augmentation followed by asymptotic convergence toward a stable value under increasing hydrostatic conditions. In the linear viscoelastic model, by contrast, the static modulus does not change with depth. Hence, as depth increases, the maximum elastic deformation in the linear viscoelastic model increases progressively. Moreover, under the present simulation conditions, the maximum elastic deformation in the linear viscoelastic model is always greater than that in the visco-hyperelastic model, and the difference between the two grows with depth, as shown in Figure 6b.

It should be noted that although the maximum fluid pressure and the proportion of contact load exhibit relatively small discrepancies between the linear viscoelastic model and the visco-hyperelastic model, with the maximum relative error in fluid pressure reaching only 0.59% and the maximum relative error in contact load proportion amounting to 1.83% at a seawater depth of 1000 m, the maximum relative error in elastic deformation between the two models reaches 19.79%, attributable to the significant difference in elastic modulus.

Figure 7 compares the water-film stiffness coefficients of both the linear viscoelastic and visco-hyperelastic frameworks at different seawater depths. With increasing depth, the radial clearance of the bearing and seawater viscosity rise simultaneously. A reduction in radial clearance will lead to an increase in water-film thickness, thereby reducing the water-film stiffness coefficient, whereas an increase in seawater viscosity will enhance

the water-film stiffness coefficient. Under the combined action of these two factors, k_{xx} and k_{zx} decrease gradually with increasing depth, while k_{xz} and k_{zz} first increase and then decrease as depth increases. In addition, at smaller depths, the linear viscoelastic model yields larger k_{xx}, k_{xz}, and k_{zz} than the visco-hyperelastic model, whereas when the depth exceeds 300 m, the visco-hyperelastic model exhibits larger k_{xx}, k_{xz}, and k_{zz}, as illustrated in Figure 7a,b,d. For k_{zx}, the value given by the linear viscoelastic model is close to that of the visco-hyperelastic model at a depth of 0 m, but at all other depths it is smaller than that of the visco-hyperelastic model. It should also be noted that, with increasing depth, the differences between the two models in k_{xx}, k_{xz}, k_{zx}, and k_{zz} grow progressively.

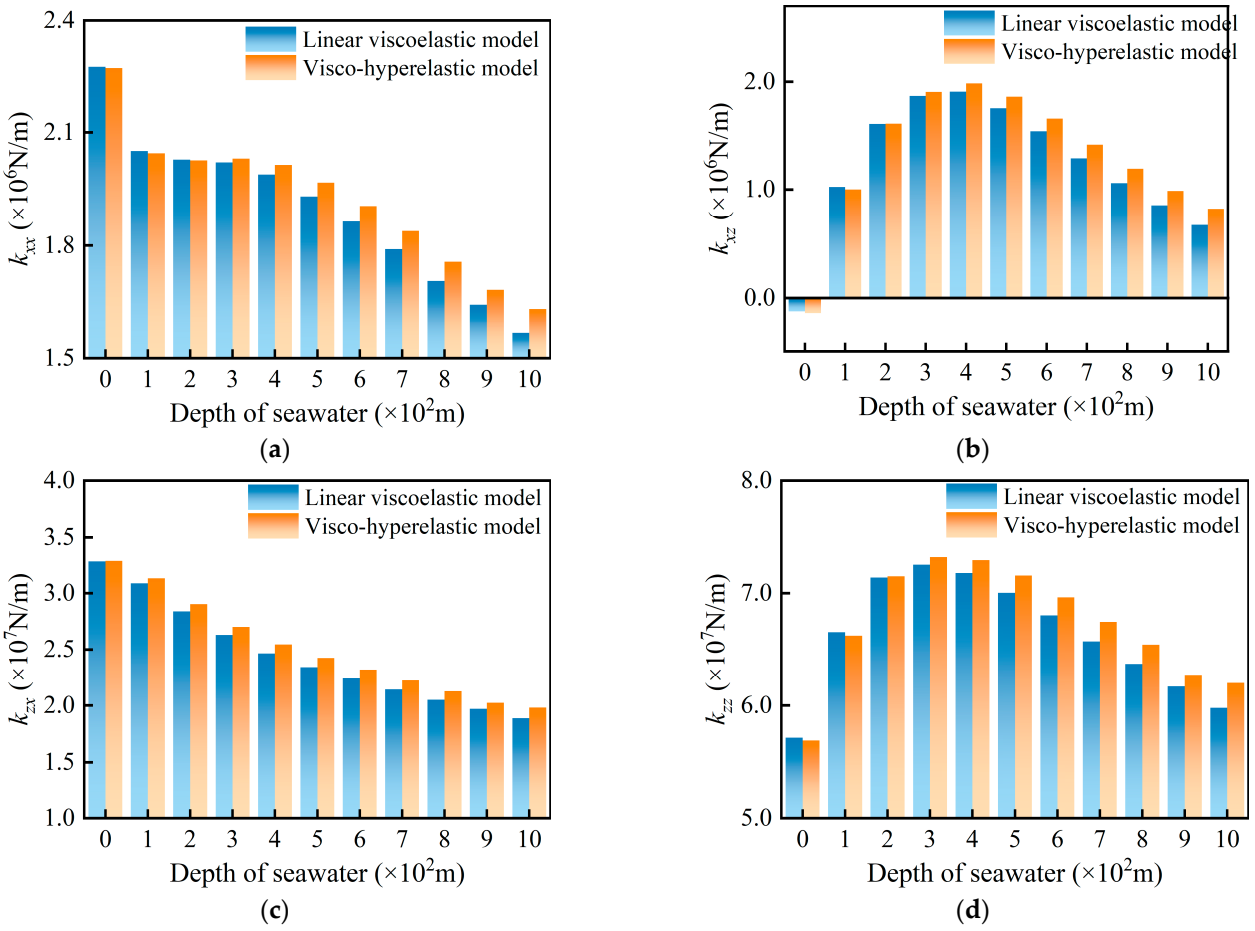


Figure 7. Comparison of the water-film stiffness coefficients between the linear viscoelastic model and the visco-hyperelastic model across different seawater depths: (**a**) k_{xx}; (**b**) k_{xz}; (**c**) k_{zx}; (**d**) k_{zz}.

Furthermore, at a water depth of 1000 m, the relative errors of k_{xx}, k_{xz}, k_{zx}, and k_{zz} for the linear viscoelastic model and the visco-hyperelastic model reach their maximum values, amounting to 4.02%, 18.41%, 4.68%, and 3.56%, respectively. It can thus be concluded that accounting for the hyperelastic characteristics of rubber materials has the most significant influence on k_{xz} and the least on k_{zz} in water-lubricated rubber bearings.

In summary, the stiffness characteristics of the water film in rubber bearings lubricated by seawater operating at different seawater depths exhibit pronounced differences. Furthermore, the comparative analysis of both the linear viscoelastic and visco-hyperelastic approaches shows that neglecting rubber hyperelasticity will lead to erroneous assessments of mixed-lubrication performance and of the stiffness parameter of the lubricating water film in rubber bearings. Therefore, when analysing the stiffness properties of the water film in these bearings, the effects of seawater depth and hyperelasticity should be taken into account.

3.3. Effect of Rotational Speed on the Stiffness of Water Film

Figure 8 illustrates how the water-film stiffness coefficients of water-lubricated rubber bearings change with seawater depth under different rotational speeds. At the same rotational speed, as seawater depth increases, k_{xx} and k_{zx} decrease progressively, whereas k_{xz} and k_{zz} first increase and then decrease. An increase in rotational speed strengthens the hydrodynamic effect, increasing the load-carrying capacity of the water film and its resistance to deformation; that is, the water-film stiffness coefficient increases. Therefore, at the same depth, k_{xx}, k_{zx}, k_{xz}, and k_{zz} all increase with rotation velocity, as illustrated in Figure 8a–d. Moreover, it is clear that at low rotational velocity, a rise in speed has a larger impact on k_{xx}, k_{zx}, k_{xz}, and k_{zz}, whereas at higher speeds the influence of speed on the water-film stiffness coefficient weakens. It should also be noted that when the depth is small, the influence of speed on k_{xz} is minor, but increasing speed raises the inflection point of the variation of k_{xz} with depth.

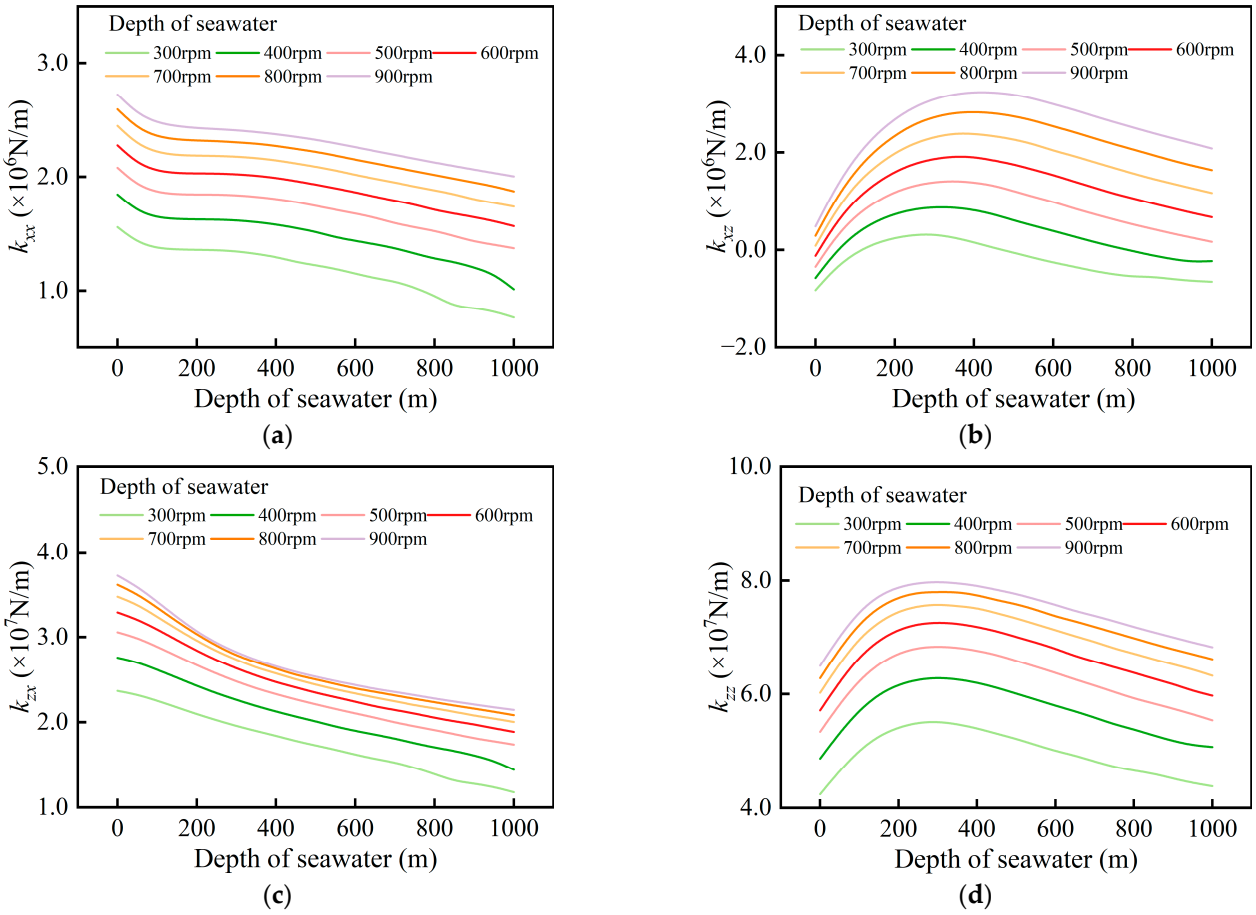


Figure 8. Variation patterns of water-film stiffness coefficients in water-lubricated rubber bearings under different rotational speeds with respect to seawater depth: (**a**) k_{xx}; (**b**) k_{xz}; (**c**) k_{zx}; (**d**) k_{zz}.

Figure 9 illustrates how the critical mass of water-lubricated rubber bearings varies with the eccentricity ratio at different seawater depths. As shown in Figure 9, with increasing depth, the dimensionless critical-mass coefficient of bearings at lower eccentricity ratios decreases progressively. In addition, at the same depth, the dimensionless critical-mass coefficient of a water-lubricated rubber bearing first increases, then decreases, and then increases again with increasing eccentricity ratio, ultimately attaining absolute stability. In sum, at smaller eccentricity ratios, increasing depth reduces the critical mass of water-lubricated rubber bearings and diminishes system stability.

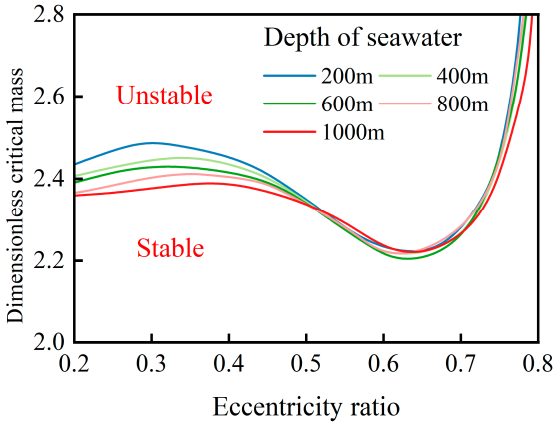


Figure 9. Variation patterns of the critical mass in water-lubricated rubber bearings with respect to eccentricity under different seawater depths.

4. Conclusions

Herein, using the proposed visco-hyperelastic mixed-lubrication model, this study examines how the water-film stiffness coefficient evolves with seawater depth, considering both deep-sea conditions and the visco-hyperelastic characteristics of rubber. The main conclusions are as follows:

(1) The water-film stiffness coefficients obtained from the linear viscoelastic and visco-hyperelastic models exhibit significant discrepancies, with the divergence increasing progressively with seawater depth. At a depth of 1000 m, the relative error in k_{xz} between the two models reaches as high as 18.41%, underscoring the importance of accounting for visco-hyperelastic behavior in accurately predicting the dynamic characteristics of the water film in deep-sea applications.

(2) Seawater depth has a pronounced effect on the water-film stiffness coefficient of water-lubricated rubber bearings. k_{xx} and k_{zx} decrease gradually with increasing depth, while k_{xz} and k_{zz} first increase and then decrease as depth increases. Therefore, the influence of depth should be considered when analyzing the water-film stiffness coefficient.

(3) Increasing rotational speed strengthens the hydrodynamic effect and enhances the water-film stiffness coefficient. However, the influence of the rotational speed on the water-film stiffness coefficient is more significant at lower speeds and weaker at higher speeds.

(4) Increasing seawater depth reduces the critical mass of water-lubricated rubber bearings at low eccentricity ratios, thereby degrading bearing stability.

Due to current experimental constraints, this study has not yet carried out comparative measurements of the water-film stiffness coefficients of water-lubricated rubber bearings. This aspect will be further investigated in future work when suitable experimental conditions are available. In addition, it is necessary to extend the current theoretical model by developing a friction-induced vibration model for water-lubricated rubber bearings under mixed lubrication. Such a model will enable the analysis of how the visco-hyperelastic properties of rubber and the seawater environment affect the stability of friction-induced vibrations.

Author Contributions: Methodology, L.W. and Q.Z.; Software, L.W.; Validation, L.W.; Formal analysis, L.W. and Q.Z.; Investigation, L.W. and Q.Z.; Data curation, L.W. and Q.Z.; Writing—original draft, L.W. and Q.Z.; Writing—review & editing, W.F. and G.X.; Supervision, W.F. and G.X.; Project administration, W.F. and G.X.; Funding acquisition, W.F. and G.X. All authors have read and agreed to the published version of the manuscript.

Funding: The present study was funded by the National Natural Science Foundation of China (No. 52305183 and No. 52105052), the Natural Science Foundation Project of Chongqing, China (CSTB2023NSCQ-MSX0035), the China Postdoctoral Science Foundation (2023M740422), and the Science and Technology Research Program of Chongqing Municipal Education Commission (No. KJQN202201508, KJQN202301547).

Data Availability Statement: The original contributions presented in this study are included in the article. Further inquiries can be directed to the corresponding authors.

Conflicts of Interest: Please add the corresponding content of this part.

References

1. Liu, Z.; Liu, K.; Chen, X.; Ma, Z.; Lv, R.; Wei, C.; Ma, K. Deep-sea rock mechanics and mining technology: State of the art and perspectives. *Int. J. Min. Sci. Technol.* **2023**, *33*, 1083–1115. [CrossRef]
2. Zhang, Q.; Chen, X.; Luan, L.; Sha, F.; Liu, X. Technology and equipment of deep-sea mining: State of the art and perspectives. *Earth Energy Sci.* **2025**, *1*, 65–84. [CrossRef]
3. Zhou, G.W.; Wu, K.P.; Pu, W.; Li, P.; Han, Y.F. Tribological modification of hydrogenated nitrile rubber nanocomposites for water-lubricated bearing of ship stern shaft. *Wear* **2022**, *504–505*, 204432. [CrossRef]
4. Litwin, W. Water-lubricated bearings of ship propeller shafts—Problems, experimental tests and theoretical investigations. *Pol. Marit. Res.* **2009**, *16*, 41–49. [CrossRef]
5. Geng, T.; Meng, Q.; Wang, N.; Yuan, X.; Jia, Q. Experimental investigation of film pressure distribution in water-lubricated rubber journal bearings. *Proc. Inst. Mech. Eng. Part J J. Eng. Tribol.* **2013**, *228*, 397–406. [CrossRef]
6. Litwin, W. Influence of main design parameters of ship propeller shaft water-lubricated bearings on their properties. *Pol. Marit. Res.* **2010**, *4*, 39–45. [CrossRef]
7. Lun, W.; Zhou, X.C.; Zhu, H.H.; Huang, Q.P.; Zhou, Z.J.; Xing, S.P.; Liu, X.S. Fluid–Structure Interaction Mechanisms of Layered Thickness Effects on Lubrication Performance and Energy Dissipation in Water-Lubricated Bearings. *Lubricants* **2025**, *13*, 445. [CrossRef]
8. Gong, J.; Jin, Y.; Liu, Z.; Jiang, H.; Xiao, M. Study on influencing factors of lubrication performance of water-lubricated micro-groove bearing. *Tribol. Int.* **2019**, *129*, 390–397. [CrossRef]
9. Sander, D.E.; Allmaier, H.; Priebsch, H.H.; Witt, M.; Skiadas, A. Simulation of journal bearing friction in severe mixed lubrication—Validation and effect of surface smoothing due to running-in. *Tribol. Int.* **2016**, *96*, 173–183. [CrossRef]
10. Deng, X.; Gates, H.; Fittro, R.; Wood, H. Methodology of Turbulence Parameter Correction in Water-Lubricated Thrust Bearings. *J. Fluids Eng.* **2019**, *141*, 071104. [CrossRef]
11. Deng, X. Study of Temperature Drop Region in Transitional Region in Fluid-Film Thrust Bearings. *J. Fluids Eng.* **2024**, *146*, 121201. [CrossRef]
12. Deng, X. A Mixed Zero-Equation and One-Equation Turbulence Model in Fluid-Film Thrust Bearings. *J. Tribol.* **2023**, *146*, 034101. [CrossRef]
13. Lv, F.R.; Zhang, X.J.; Ji, C.C.; Rao, Z.S. Theoretical and experimental investigation on local turbulence effect on mixed-lubrication journal bearing during speeding up. *Phys. Fluids* **2022**, *34*, 113104. [CrossRef]
14. Lv, F.R.; Shangguan, Y.; Zou, D.; Ji, A. Transient mixed-lubrication analysis of low-viscosity lubricated bearings under impact load with consideration of turbulence. *Phys. Fluids* **2022**, *34*, 033108. [CrossRef]
15. Ouyang, W.; Zhang, Z.; Nie, Y.; Liu, B.; Vanierschot, M. Parametric modeling and collaborative optimization of a rim-driven thruster considering propeller-duct interactions. *Ocean. Eng.* **2025**, *337*, 121746. [CrossRef]
16. Ouyang, W.; Liu, Q.; Li, J.; Jin, Y.; Dong, X. Semi-active control for transverse vibration of ship propulsion shafting with magnetorheological squeeze film damper. *Mech. Syst. Signal Process.* **2025**, *233*, 112763. [CrossRef]
17. Xie, Z.; Zhang, Y.; Zhou, J.; Zhu, W. Theoretical and experimental research on the micro interface lubrication regime of water lubricated bearing. *Mech. Syst. Signal Process.* **2021**, *151*, 107422. [CrossRef]
18. Xie, Z.; Liu, H. Experimental research on the interface lubrication regimes transition of water lubricated bearing. *Mech. Syst. Signal Process.* **2020**, *136*, 106522. [CrossRef]
19. Han, Y.F.; Tang, T.; Xiang, G.; Jia, H. A Fluid–Solid–Heat Coupling Analysis for Water-Lubricated Rubber Stern Bearing Considering the Deflection of Propeller Shaft. *Appl. Sci.* **2021**, *11*, 1170. [CrossRef]
20. Song, Y.; Xiao, K.; Xiang, G. Entropy-based fluid–solid–thermal coupled wear prediction of journal bearing during repeated starting and stopping. *Wear* **2024**, *536–537*, 205157. [CrossRef]
21. Zhao, Z.; Zhang, R. Theoretical and experimental analysis of a water-lubricated rubber journal bearing with a large aspect ratio. *Ind. Lubr. Tribol.* **2019**, *72*, 797–803. [CrossRef]

22. Wu, C.; Wang, Y.; Chen, F.; Long, X. A mixed-lubricated friction model of water lubricated bearing based on fractal theory. *Proc. Inst. Mech. Eng. Part J J. Eng. Tribol.* **2023**, *237*, 1913–1929. [CrossRef]
23. Ouyang, W.; Liu, Q.; Liang, X.; Zhang, X.; Wang, W. Data-Driven Model of the Distribution Lubrication on Water-Lubricated Bearing Under Severe Operating Conditions. *J. Tribol.* **2023**, *237*, 1913–1929. [CrossRef]
24. Shen, Y.; Zhang, Y.; Zhang, X.; Zheng, H.; Wei, G.W.; Wang, M. A Fluid-Structure Interaction Method for the Elastohydrodynamic Lubrication Characteristics of Rubber-Plastic Double-Layer Water-Lubricated Journal Bearings. *Lubricants* **2023**, *11*, 240. [CrossRef]
25. Kuang, F.; Mu, H.; Huang, J.; Wan, G.; Yuan, C.; Zhou, X. Theoretical and In Situ High Speed Measurement Study on Friction-Induced Vibration in Water Lubricated Rubber Bearing-Shaft System. *Tribol. Trans.* **2024**, *67*, 47–61. [CrossRef]
26. Chen, R.; Zhao, B.; Xin, Q.; Niu, X.; Xie, Z.; Lu, X.; Zou, D. Analysis of transient lubrication and wear coupling behaviors considering thermal effect and journal misalignment for main bearings under dynamic load. *Wear* **2024**, *554-555*, 205478. [CrossRef]
27. Shi, J.; Zhao, B.; Niu, X.; Xin, Q.; Xu, H.; Lu, X. Time-varying dynamic characteristic analysis of journal–thrust coupled bearings based on the transient lubrication considering thermal-pressure coupled effect. *Phys. Fluids* **2024**, *36*. [CrossRef]
28. Xiang, G.; Goltsberg, R.; Etsion, I. Modeling static friction behavior of elastic–plastic spherical adhesive microcontact in full-stick condition. *Friction* **2024**, *12*, 2594–2610. [CrossRef]
29. Yang, T.Y.; Xiao, K.; Xiang, G.; Wang, L.W.; Cai, J.L.; Wang, J.X. Effects of rotating microgroove on tribo-dynamic performance of coupled bearings. *Int. J. Mech. Sci.* **2024**, *279*, 109629. [CrossRef]
30. Grosch, K.A. The relation between the friction and visco-elastic properties of rubber. *Proc. R. Soc. London. Ser. A Math. Phys. Sci.* **1963**, *274*, 21–39. [CrossRef]
31. Schallamach, A. How Does Rubber Slide? *Wear* **1971**, *17*, 301–312. [CrossRef]
32. Wang, L.; Xiang, G.; Han, Y.; Yang, T.; Zhou, G.; Wang, J. A mixed visco-hyperelastic hydrodynamic lubrication model for water-lubricated rubber bearings. *Int. J. Mech. Sci.* **2025**, *286*, 109887. [CrossRef]
33. Wang, L.; Xiao, K.; Xiang, G.; Cai, J.; Yang, T.; Wang, J. Study on mixed thermal-visco-hyerelastic hydrodynamic lubrication performance of water-lubricated rubber bearings in deep-sea environment. *Tribol. Int.* **2025**, *209*, 110713. [CrossRef]
34. Luo, W.-b.; Sheng, L.; Yong-jun, Z. Fractional Differential Constitutive Model for Dynamic Viscoelasticity of Asphalt Mixture. *China J. Highw. Transp.* **2020**, *33*, 34–43. [CrossRef]
35. Persson, B. Theory of rubber friction and contact mechanics. *J. Chem. Phys.* **2001**, *115*, 3840–3861. [CrossRef]
36. Persson, B.; Albohr, O.; Tartaglino, U.; Volokitin, A.; Tosatti, E. On the nature of surface roughness with application to contact mechanics, sealing, rubber friction and adhesion. *J. Phys. Condens. Matter Inst. Phys. J.* **2005**, *17*, R1–R62. [CrossRef]
37. Carbone, G.; Mangialardi, L. Analysis of the adhesive contact of confined layers by using a Green's function approach. *J. Mech. Phys. Solids* **2008**, *56*, 684–706. [CrossRef]
38. Carbone, G.; Lorenz, B.; Persson, B.N.J.; Wohlers, A. Contact mechanics and rubber friction for randomly rough surfaces with anisotropic statistical properties. *Eur. Phys. J. E* **2009**, *29*, 275–284. [CrossRef] [PubMed]
39. Carbone, G.; Putignano, C. A novel methodology to predict sliding and rolling friction of viscoelastic materials: Theory and experiments. *J. Mech. Phys. Solids* **2013**, *61*, 1822–1834. [CrossRef]
40. Patir, N.; Cheng, H.S. An Average Flow Model for Determining Effects of Three-Dimensional Roughness on Partial Hydrodynamic Lubrication. *J. Lubr. Technol.* **1978**, *100*, 12–17. [CrossRef]
41. Wu, C.; Zheng, L. An Average Reynolds Equation for Partial Film Lubrication With a Contact Factor. *J. Tribol.* **1989**, *111*, 188–191. [CrossRef]
42. Dingcheng, X.; Yipan, D.; Zhengyao, W.; Tianhao, L.; Yinshui, L. Viscosity evolution of water glycol in deep-sea environment at high pressure and low temperature. *J. Mol. Liq.* **2023**, *387*, 122387. [CrossRef]
43. Kuznetsov, E.; Glavatskih, S.; Fillon, M. THD analysis of compliant journal bearings considering liner deformation. *Tribol. Int.* **2011**, *44*, 1629–1641. [CrossRef]
44. Skotheim, J.M.; Mahadevan, L. Soft lubrication. *Phys. Rev. Lett.* **2004**, *92*, 245509. [CrossRef]
45. Skotheim, J.; Mahadevan, L. Soft lubrication: The elastohydrodynamics of nonconforming and conforming contacts. *Phys. Fluids* **2005**, *17*, 092101. [CrossRef]
46. Bernard, J.; Hamrock, S.R. *Fundamentals of Fluid Film Lubrication*; CRC Press: Boca Raton, FL, USA, 2004.
47. Hartoko, A. Spatial Distribution of *Thunnus* sp., Vertical and Horizontal Sub-Surface Multilayer Temperature Profiles of In-Situ Agro Float Data in Indian Ocean. *J. Coast. Zone Manag.* **2010**, *14*, 61–74.

Disclaimer/Publisher's Note: The statements, opinions and data contained in all publications are solely those of the individual author(s) and contributor(s) and not of MDPI and/or the editor(s). MDPI and/or the editor(s) disclaim responsibility for any injury to people or property resulting from any ideas, methods, instructions or products referred to in the content.